Electronic Supplementary Material (ESI) for Materials Horizons.

Supplementary material

Perfect Absorption Based on Ceramic Anapole Metamaterial

Weijia Luo[1], Xubin Wang[2], Xingcong Chen[1], Siyong Zheng[1], Shiqiang Zhao[1], Yongzheng Wen[1], Lingxia Li[†,2], Ji Zhou[††,1]

1. State Key Laboratory of New Ceramics and Fine Processing, School of Materials Science and Engineering, Tsinghua University, Beijing 100084, China

2. School of Microelectronics, Tianjin University, Tianjin 300072, China

In order to compare the coupling difference between the environment in waveguides and in free space for meta-atoms, the electric field distribution and phase relationship is studied in advance. At the excitation frequencies of hybrid anapole modes in both free space and waveguides conditions, the electric field distribution and the Smith chart are exhibited in Fig.S1A and S1B. Near the perfect absorption frequency, the electric field is localized around the meta-atoms in both free space and waveguides. Especially in the gap between meta-atoms or meta-atom and the inner wall of waveguides, enhancement of electric field is clearly observed, as additional capacitive effect. And inside the meta-atom, adjusting their reasonable Q*f* values (6200GHz in free space and 11000GHz in waveguides) with fixed coupling conditions, the electric field distribution become very similar, indicating nearly same hybrid mode excitation. Meanwhile, in the Smith chart in Fig.S1C and S1D, impedance matching as the prerequisite for absorption, can be also obtained approximately at the excitation frequency in both S11 and S21 parameters, as $Z = \sqrt{\frac{[1+R(\omega)]^2 - T(\omega)^2}{[1-R(\omega)]^2 - T(\omega)^2}} = \sqrt{\frac{(1+S11)^2 - S21^2}{(1-S11)^2 - S21^2}} \approx 1$, and the rationality of hybrid anapole modes under different conditions here is verified.

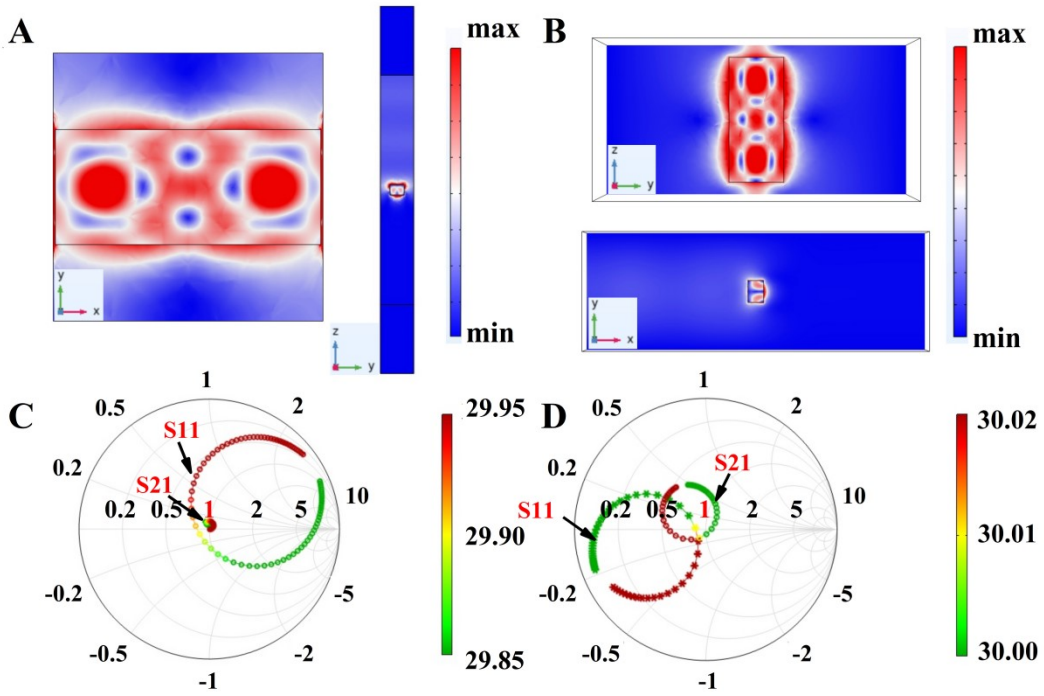

Figure.S1 (A) E-field distribution of metamaterial perfect absorber in free space, (C) the corresponding smith chart for impedance analysis. (B) E-field distribution of meta-atom in waveguides for verification, (D) the corresponding smith chart for impedance analysis.

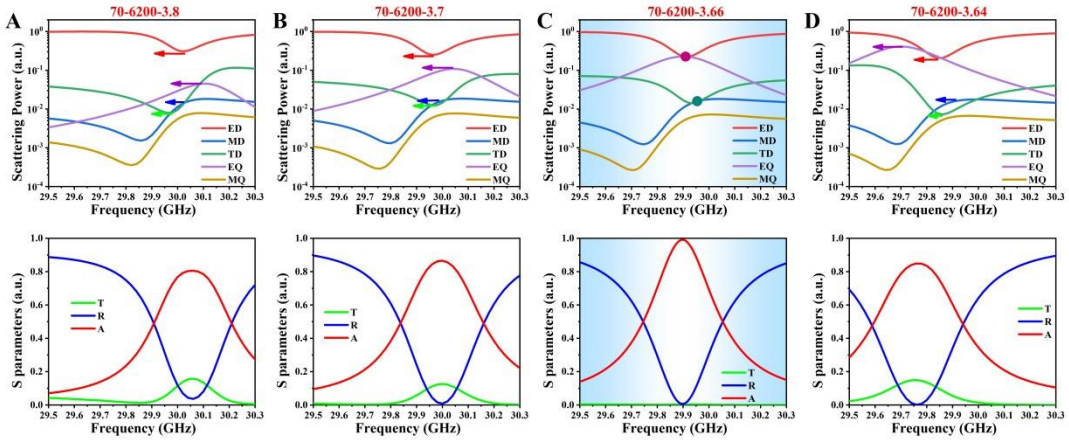

Figure.S2 (A~D) Above: correlation between period (coupling distance) and scattering energy in multipole decomposition process. Below: the corresponding simulated transmittance, reflectance and absorbance.

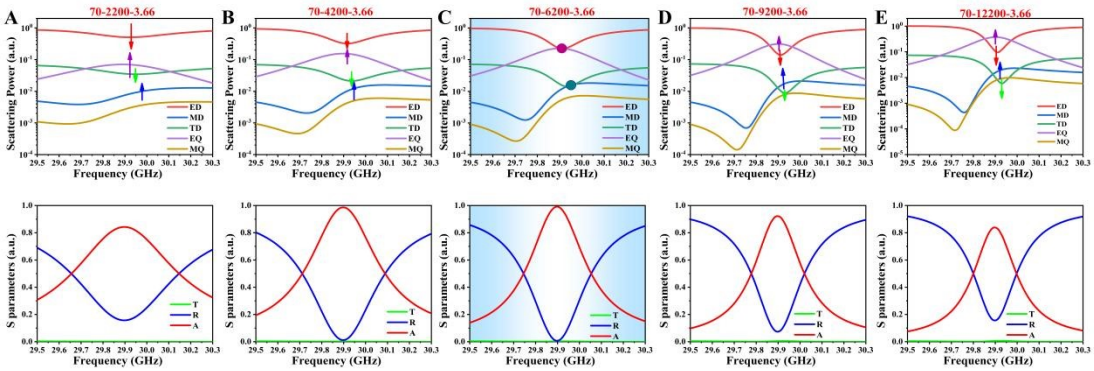

Figure.S3 (A~E) Above: correlation between Q*f* value and scattering energy in multipole decomposition process. Below: the corresponding simulated transmittance, reflectance and absorbance.

XRD and SEM analysis

The XRD analysis results of BENT-AG (x=0, 1, 2, 3) ceramics are presented in Fig.S4. All the samples crystallize as a tungsten-bronze type structure with space group Pbnm (JCPDS No.89-4356) and no impurity phases are detected, which confirmed that Eu^{3+} and $(Al_{0.4}Ga_{0.6})^{3+}$ are compatible in this system. Then the Rietveld refinement is conducted to study the influence of Eu^{3+} ions on crystal structure and lattice parameters of BENT-AG ceramics. The results of Rietveld refinement (in Fig.S4 and Table S1) show the volume of unit cell decreased from V=2097.463 $Å^3$ to V=2083.306 $Å^3$, that attributed to the radius of Eu^{3+} (ionic radius = 1.004 Å) is smaller than that of Nd^{3+} (ionic radius = 1.109 Å) under the same coordination environment. Intuitively, with more Eu^{3+} ions successfully entered the lattice as x increased, the volume of unit cell gradually shrinked. Meanwhile, the influence of Eu^{3+} substitution on microstructure and element distribution is detected by scanning electron microscopy (SEM) and energy dispersive spectroscopy (EDS), the results are shown in Fig.S4B. Obviously, dense microstructure and typical rod-like grains in all samples are exhibited, the distribution of Eu^{3+} ions in all samples is very uniform according to the EDS mapping, also corroborating the XRD analysis.

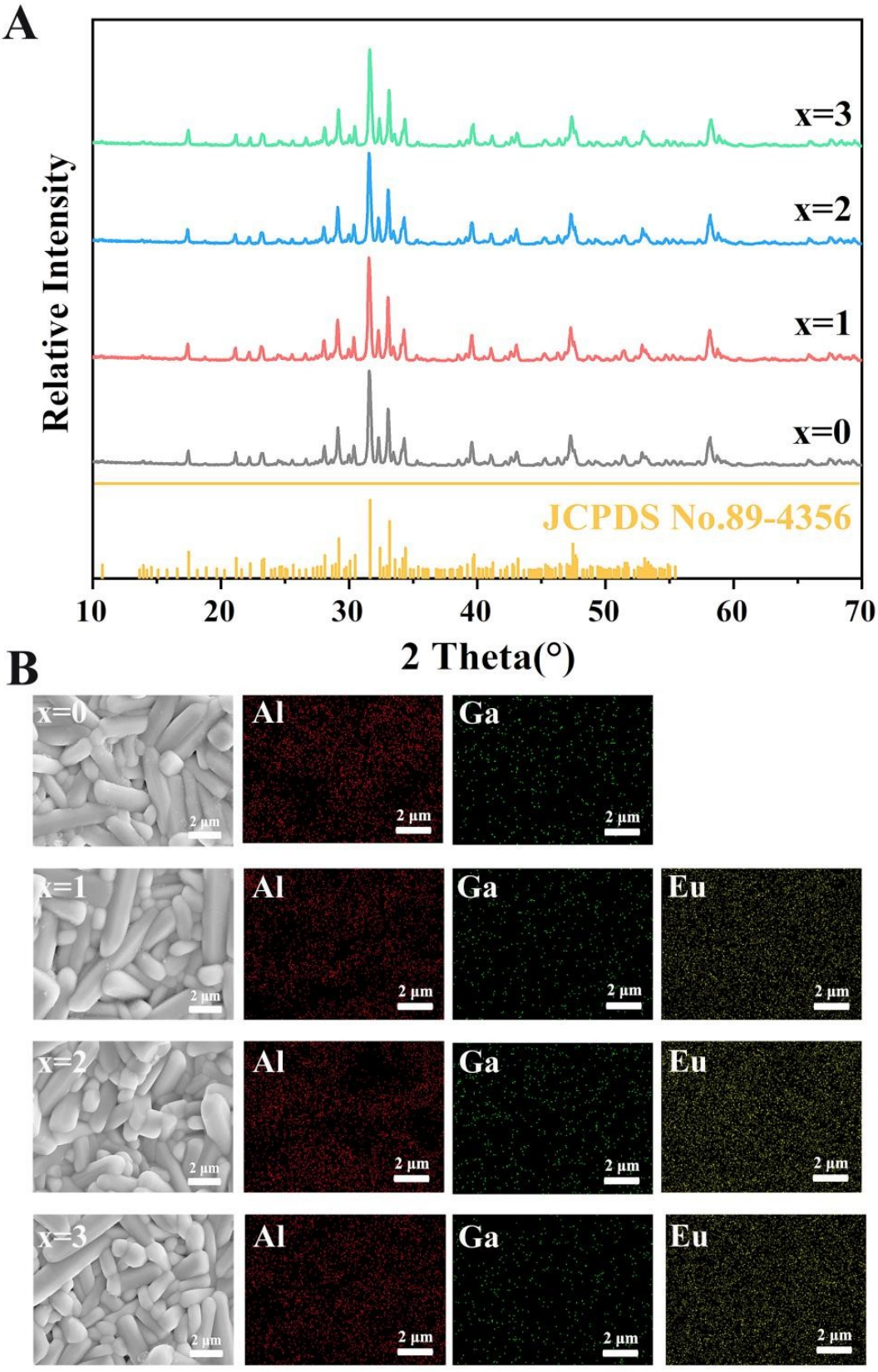

Figure.S4 (A) XRD patterns and (B) SEM images with EDS results of the BENT-AG ($0 \leq x \leq 3$) ceramics.

The Rietveld refinement method is to discretize the diffraction intensity (Y_o) of a certain 2θ interval in the entire spectrum to obtain $2\theta_i$-Y_{oi} data. Based on the initial crystal structure, the intensity value Y_{oi} corresponding to $2\theta_i$ is calculated according to the structural parameters and peak shape parameters, and the difference between the calculated value and the experimental value is minimized by the least square method, so as to obtain the modified crystal structure parameters and peaks shape information. The main structural parameters involved in the correction of the Rietveld method are structural parameters (such as unit cell parameters, atomic coordinates, atomic occupancy fractions) and peak shape parameters (such as peak width parameters, asymmetric parameters, dorsal parameters, optimal orientation parameters), which are released and corrected in a reasonable order. In order to judge whether the adjustment of parameters in the refinement process was appropriate, the R factors are designed as the numerical criterion according to the calculated spectral data and experimental spectral data, among which the R_p and R_{wp} can better reflect the fitting quality and can be calculated as the following formula:

$$R_P = \frac{\sum |Y_{oi} - Y_{ci}|}{\sum Y_{oi}} \tag{S1}$$

$$R_{wp} = \sqrt{\frac{W_i (Y_{oi} - Y_{ci})^2}{W_i Y_{oi}^{\ 2}}} \tag{S2}$$

where W_i is the weight factor based on statistics, Y_{oi} is the experimental value and Y_{ci} is the calculated value. R_p and R_{wp} are the profile R factor and weighted profile R factor, reflecting the merits and disadvantages of fitting, respectively. Generally, when the R factors are less than 15%, the result of refinement is reliable. The results of Rietveld refinement are shown in Fig.S5 and Table S1.

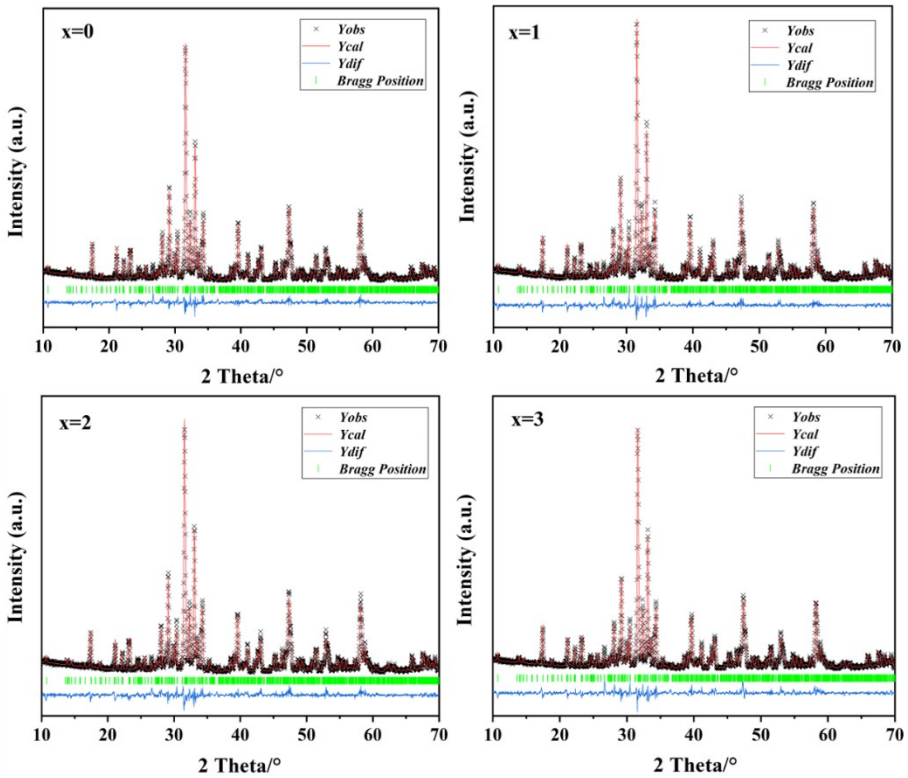

Figure.S5 Rietveld refinement process of BENT-AG ceramics, x = 0~3.

Table S1 Lattice parameters and cell volumes versus compositions in the BENT-AG ceramics

x	0	1	2	3
a(Å)	12.1983	12.1810	12.1738	12.1601
b(Å)	22.3624	22.3489	22.3458	22.3311
c(Å)	7.6891	7.6778	7.6736	7.6626
V(Å^3)	2097.463	2090.146	2087.467	2080.767
R_{wp}	10.72	10.42	11.00	11.62
R_p	7.92	7.76	8.37	8.71
χ^2	2.061	2.179	2.297	2.524
Theoretical/Bulk density (g/cm^3)	5.826/5.688	5.846/5.702	5.854/5.739	5.872/5.730
Relative density (%)	97.63	97.54	98.04	97.58

Experimental procedure

The BENT-AG (x=0, 1, 2, 3, 4) samples are synthesized by the solid-phase reaction process. High-purity powders of $BaCO_3$ (99.8%, Yuanli, Tianjin, China), Nd_2O_3 (99.99%, Hengshan, Tianjin, China), TiO_2 (99%, Pengda, Jinzhou, China), Al_2O_3 (99.99%, Aladdin, Shanghai, China), Eu_2O_3 (99.99%, Energy Chemical, Anhui, China) and Ga_2O_3 (99.999%, Mreda, Beijing, China) are used as the raw material and weighted according to certain proportion. After mixed with anhydrous ethanol, the powders are ball-milled in nylon jars for 6h with yttria-stabilized zirconia balls, and calcined at 1185 ℃ for 5h. Then the calcined mixtures are re-milled for 12 h after mixed with deionized water and 1 wt% PVA addition, followed by pressing into cylinders and sintering in air at a heating rate of 5 ℃/min to 1300 ℃ and held for 6 hours. The specific process is shown in the following Fig.S6.

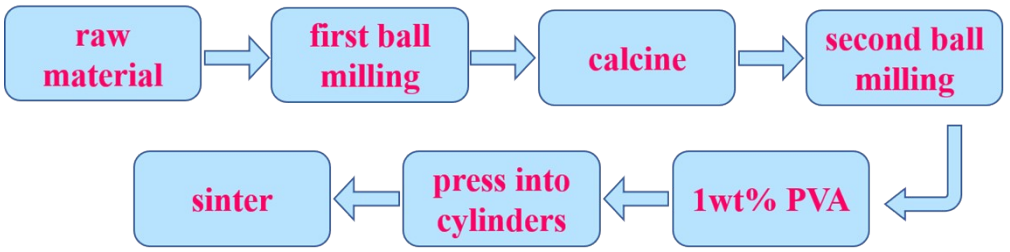

Figure.S6 Preparation procedure of BENT-AG ceramics.

Raman analysis

Fig. S7 shows the Raman spectra of the BENT-AG ceramics in the range of 100cm^{-1} ~ 900cm^{-1}. Theoretically, 252 Raman active modes ($71A_g + 55B_{1g} + 71B_{2g} + 55B_{3g}$) are predicted according to group theory and D_{2h} point group, and only 12 Raman active modes can be calibrated, which is due to the symmetry that most predicted modes are broadened and hidden, or the vibration may not be sufficient to produce observable Raman peaks. Considering the symmetry of BENT-AG ceramics with tungsten bronze structure, $\Gamma_{Raman} = 71A_g + 55B_{1g} + 71B_{2g} + 55B_{3g}$. Here, the vibrational modes are marked by dotted line at 118cm^{-1}, 143cm^{-1}, 192cm^{-1}, 235cm^{-1}, 283cm^{-1}, 305cm^{-1}, 336cm^{-1}, 405cm^{-1}, 438cm^{-1}, 532cm^{-1}, 593cm^{-1}, and 751cm^{-1} respectively. In the high wave number region, the modes around 532cm^{-1}, 593cm^{-1} and 751cm^{-1} are attributed to the symmetric stretching vibration of Ti-O bonds, determined as $A_{g(2)}$, B_{1g} and $A_{g(1)}$ respectively. Then the mode at 404cm^{-1} is associated with the bending vibration of Ti–O bonds and the modes in the region of 200cm^{-1} ~ 300cm^{-1} mainly reflect the tilt and rotation of the oxygen octahedron. With the increase of Eu^{3+} ions, it can be seen that the changes of Raman peaks between 400cm^{-1} ~ 800cm^{-1} are not significant, indicating the little effect on Ti-O vibration. Moreover, the intensified 305 cm^{-1} and 366 cm^{-1} peaks partially demonstrates the increasing tilt degree of oxygen octahedra with the substitution of Eu^{3+}.

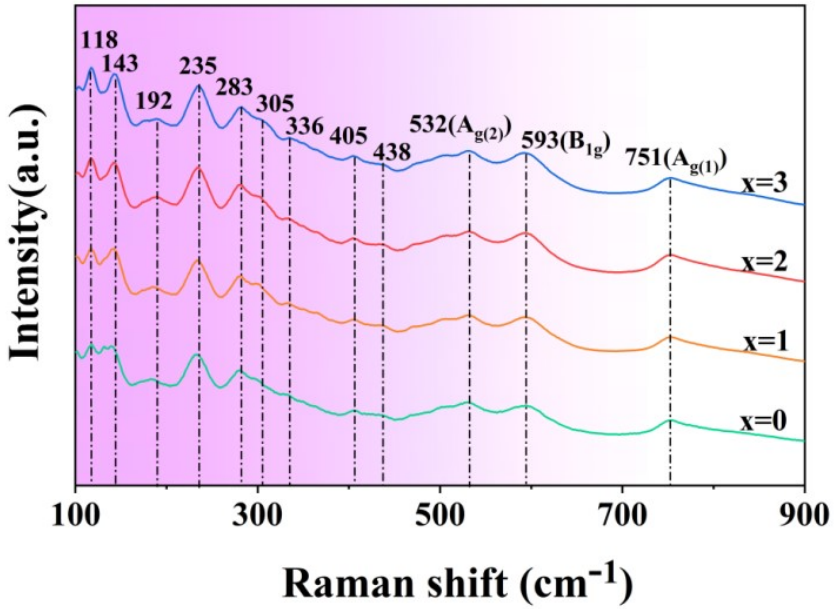

Figure.S7 Raman spectra of BENT-AG ceramics.

GII calculation and dielectric properties of BENT-AG ceramics

Here, Clausius-Mosotti equation can be expressed the relationship between dielectric constant and polarizability, as shown in equation (S3):

$$\varepsilon_{rc} = \frac{3V_m + 8\pi\alpha_D}{3V_m - 4\pi\alpha_D} \quad \text{(S3)}$$

Where α_D is the sum of the dielectric polarizabilities of all ions, V_m is molar volume and ε_{rc} is theoretical dielectric constant. As reported by Shannon, the molecular polarizabilities of complex substances can be broken up into the polarizabilities of constituent ions and the total theoretical polarizability in BENT-AG can be calculated by the following equation (S4):

$$\alpha_D(BENT-AG) = \left[\alpha(Ba^{2+}) \times 4 + \alpha(Eu^{3+}) \times x + \alpha(Nd^{3+}) \times (9.33-x) + \alpha(Ti^{4+}) \times \right. \\ \left. \times 2\right. \quad \text{(S4)}$$

Where α_D is the theoretical molecular polarizability and the results (4.53 Å^3 for Eu^{3+} and 5.01 Å^3 for Nd^{3+} [1]) are listed in table S2. Although the

anisotropy in the ion's coordination environment leads to numerical deviation between the ε_r and ε_{rc}, the value of the ε_{rc} represents a decreasing tendency which is consistent with ε_r when x varies from 1 to 3, indicating the correlation between the dielectric polarizabilities and ε_r is still convincing and dielectric polarizabilities dominate the decrease of ε_r.

Since the extrinsic factors of BENT-AG ceramics are similar, such as the secondary phase, microstructural characteristics, and density, the $Q \times f$ is mainly determined by intrinsic loss here. It has been reported that the occupation of the A1 and A2 sites leads to fluctuation of d-spacing (lattice parameters) and internal strain around themselves, bringing intrinsic loss.

Global instability index (GII) can be used to correlate this effect. For the ideal unstrained structures at equilibrium, the absolute value of the oxidation state should be equal to the sum of bond valence for any ion in the thermodynamically stable phase. According to the distortion theorem, the extension or shortening of bonds will increase the sum of bond valence, the difference between the oxidation state of any atom and the sum of bond valence surrounding can be used to evaluate the internal strain associated with stability of the crystal structure.

Based on the Pauling's rules, the bond valence S_{ij} of chemical bonds could be determined by the followed empirical equation (S5):

$$S_{ij} = exp\left(\frac{D_0 - D_{ij}}{B}\right) \quad \text{(S5)}$$

Where D_0 was the length of a bond of unit valence, which had been tabulated based on plenty of experiment data. B was a constant that equal to 0.37 and D_{ij} was the length of chemical bond, respectively. Thus, the bond discrepancy factor d_i was defined as the deviation of the bond valence sum from the oxidation state V_i and could be represented as follows:

$$d_i = V_i - \sum_j S_{ij} \quad \text{(S6)}$$

The parameter d_i could be used to evaluate the state of bonds under tensile or compressive strain. The negative d_i indicated that the bonds around the ith ion were under compressive strain. Conversely, the positive d_i corresponded to the bonds were under tensile strain conditions. Then the quantitative parameter of such lattice strains over the whole structure was defined as GII, which involved all cations in the lattice and could be expressed as the root-mean-square of the d_i values:

$$GII = \sqrt{\frac{\sum_{i=1}^{N} d_i^2}{N}} \quad \text{(S6)}$$

where N was the number of ions. The GII was introduced to compare structure stability, and the larger value of GII weas indicative of more severe strained bonds which resulted in the instabilities and internal strain in crystal structure. Generally, the GII < 0.1v.u. indicated that the structure was stable and 0.1v.u. < GII < 0.2v.u. showed the bonds were excessively out of its equilibrium state in the lattice. The phenomenon with GII > 0.2v.u. only appeared in structures with low symmetry, such as the tungsten bronze structure here.

The calculation results of α_D, t, d_i, and GII of BENT-AG ceramics were listed in Table S2.

Table S2 The Microwave dielectric properties, α_D, t, d_i, and GII of BENT-AG ceramics

x	0	1	2	3
ε_r	72.1	73.9	72.7	72.3
$Q \times f$ (GHz)	10999	11811	11495	10151
τ_f (ppm/°C)	+21.9	+6.6	-4.4	-12.3
α_D	461.8086	460.8486	459.8886	458.9286
t	0.8950	0.8913	0.8876	0.8839

d_i(Ti/Al/Ga-O)	-0.4470	-0.3411	-0.3433	-0.4720
d_i(Ba-O)	-0.2137	-0.3731	-0.4787	-0.4656
d_i(Nd/Eu-O)	0.3317	0.2140	0.3711	0.2415
GII	0.2538	0.2087	0.2366	0.2808

Reference

[1] Shannon R D. (1993). Dielectric polarizabilities of ions in oxides and fluorides. Journal of Applied physics, 3(1): 348-366.